# Numerical Studies of Scattering Properties of Leaves and Leaf Moisture Influences on the Scattering at Microwave Wavelengths

Bing Lin, Wenbo Sun, Qilong Min, and Yongxiang Hu

***Abstract*—This paper uses a 3-D finite-difference time-domain method to accurately calculate the single-scattering properties of randomly oriented leaves and evaluate the influence of vegetation water content (VWC) on these properties at frequencies of 19.35 and 37.0 GHz. The studied leaves are assumed to be thin elliptical disks with two different sizes and have various VWC values. Although leaf moisture causes considerable absorption in the scattering process, the effective efficiencies of extinction and scattering of leaves essentially linearly increase with VWC, which is critical for forest remote sensing. Calculated asymmetry factors and phase functions also indicate that there is a significant amount of scattered energy at large scattering angles at microwave wavelengths. This paper can improve the modeling of the radiative transfer by vegetation canopies at the higher frequencies of the microwave spectrum, which is important for passive microwave remote sensing.**

***Index Terms*—Microwave propagation, scattering, vegetation.**

## I. Introduction

FORESTS modulate land surface and planetary boundary layer energy and hydrological budgets on local, regional, and continental scales, primarily through radiative and turbulent, particularly evapotranspiration, processes. Vegetation albedos at solar wavelengths are among the most important parameters affecting land–atmosphere radiative energy exchange [1], whereas the scattering properties of forest leaves at microwave bands are essential to understanding the evapotranspiration processes. Min and Lin [2], [3] have shown that the satellite-estimated emissivity difference vegetation index (EDVI) at microwave wavelengths is sensitive to evapotranspiration fractions of forests and, along with incoming solar radiation, is significantly correlated to evapotranspiration fluxes. The errors in estimated evapotranspiration fluxes at microwave wavelengths are much smaller than those from other operational satellite techniques. This EDVI is also an excellent empirical indicator of spring onset and growing season duration of forests due to its inherent relationship with the leaf physiology of vegetation canopy. The EDVI values are qualitatively decided by physical and biological properties of vegetation canopy [2]. More specifically, these microwave index values are directly related to the vegetation water content (VWC) (which is also called gravimetric moisture and defined as the ratio of the weight of vegetation moisture to the total weight of vegetation) of the upper layer of vegetation canopy [2]. However, the quantitative relationship between EDVI and VWC is still unknown, owing to the difficulties in the calculations of both the single- and multiple-scattering properties within vegetation canopies. Moreover, the overall emissivity is also influenced by forest geometry [4]. For irregularly shaped vegetation materials, such as forest leaves and small branches, there are no general analytical solutions for their single-scattering properties [e.g., scattering phase function, extinction and scattering cross sections, single-scattering albedo, and asymmetry factor (see Appendix B for the definitions of these parameters)]. These vegetation materials, particularly the tree leaves, are the most important contributors to the scattering and absorption at microwave wavelengths for the upper layer of vegetation canopies [2]. However, numerical calculations of broad leaves of deciduous trees at microwave wavelengths are commonly based on approximate solutions for disk-shaped particles, as shown in [5]–[7]. Accurate solutions for leaf scattering at microwave spectra are needed for forest remote sensing and vegetation canopy monitoring.

The intent of this paper is to use a 3-D finite-difference time-domain (3-D FDTD) method to numerically obtain the accurate solutions of the single-scattering properties of randomly oriented leaves, which means that the orientation of these leaves is uniformly randomly distributed over all 3-D directions. The influence of leaf moisture on the scattering is among the most important focus areas considered in this paper. The 3-D FDTD method is an accurate approach that directly solves Maxwell's equations of electromagnetic (EM) fields with arbitrarily shaped dielectric bodies imbedded in uniform media and has been used by the authors in various single-scattering calculations at visible and near-infrared wavelengths for both absorbing and nonabsorbing irregularly shaped dielectric materials [8]–[10]. This paper extends the 3-D FDTD applications to microwave spectra. Specifically, the frequencies considered here are the same as those used in EDVI calculations [2], [3] for the Special Sensor Microwave/Imager (SSM/I) measurements, i.e., 19.35 and 37.0 GHz (hereafter 19 and 37 GHz, respectively).

Manuscript received April 11, 2007; revised October 12, 2007. This work was supported by NASA's Science Mission Directorate through the Energy and Water cycle Studies (NEWS) and radiation science programs and the Clouds and the Earth's Radiant Energy System mission.

B. Lin and Y. Hu are with the Sciences Directorate, NASA Langley Research Center, Hampton, VA 23681-2199 USA (e-mail: bing.lin@nasa.gov).

W. Sun is with the Department of Atmospheric and Planetary Sciences, Hampton University, Hampton, VA 23666 USA.

Q. Min is with the Center for Atmospheric Sciences, State University of New York at Albany, Albany, NY 12222 USA.

Digital Object Identifier 10.1109/TGRS.2007.912434

The scattering calculations at these SSM/I wavelengths support forest studies using satellite remote sensing techniques. Section II discusses basic vegetation properties and the FDTD method for leaf scattering calculations. The results of the scattering calculations are presented in Section III. We summarize this paper in Section IV.

## II. Analysis Techniques

Totally dehydrated leaves of deciduous trees are generally light. Their density is only around 0.33 g/cm$^3$ and much less variable than that of leaves in normal conditions [11], [12]. The VWC of leaves generally varies from dry ($\sim$5%) to very wet ($\sim$70%) conditions [11]–[13]. The dry conditions represent senescent leaf states, whereas the much wetter cases represent fresh leaves. This moisture strongly contributes to the microwave absorption and scattering within vegetation materials. There are generally no specific models to calculate vegetation dielectric properties at frequencies higher than 20 GHz. Studies [11]–[13] show that the result of the dual-dispersion model [12] is in good agreement with experimental measurements for sampled leaves, particularly at X-band. This paper extends the dual-dispersion model to the SSM/I wavelengths (19 and 37 GHz) in the calculations of leaf dielectric properties. Room temperature is assumed for the analyzed leaves. Although there are some variations in the leaf dielectric properties with temperature, the changes are generally small [11]–[13], particularly in conditions well above the freezing point. To analyze the single-scattering characteristics of broad leaves, the leaf is assumed to have the shape of an elliptical disk. The basic size of the elliptical leaves considered is chosen to be 2.5 cm for the long semiaxis, 1.25 cm for the short semiaxis, and 0.1 cm for the thickness. Although the thickness may be higher than that of typical leaves, the assumed value may account for some thicker leaves and the potential thickening effects of nonflatness of leaves due to folds, veins, and ribs of leaves. In addition, the scattering properties of thin disks can be relatively more easily obtained from Rayleigh or other physical optical approximations, whereas those of thicker disks are more difficult for scattering calculations, as shown in [14], in which a 0.5-cm-thick disk was considered. We have also computed the scattering properties of leaves with half of the long and short semiaxes without changes in the thickness. For simplicity, hereafter, we refer to these two kinds of leaves as full size (FS) and half size (HS), respectively. Since the sizes of these assumed FS and HS leaves are comparable to the SSM/I wavelengths, particularly at 37 GHz, calculations using either geometric optics or Rayleigh–Gans approximations would produce significant errors in calculated phase functions and other scattering properties. By combining the Rayleigh–Gans approximation with geometric optics approaches, the scattering effects of elliptical disks could be calculated [15]. However, an approximation based on a solution to an infinite slab would still be used. Accurate solution techniques, such as FDTD, are critical for the computations of the scattering EM fields.

The FDTD technique with the uniaxial perfectly matched layer (UPML) absorbing boundary conditions (ABCs) [16], [17] is used to calculate the near-EM fields scattered and transmitted by leaves in the time domain. The time series at each grid point in the computational domain is calculated by updating the EM field components using the correspondence of Maxwell's equations in the finite spatial–temporal grid. The scattering and absorption quantities are calculated in the frequency domain at the end of the computation. Detailed descriptions of the FDTD technique with a UPML ABC and the basic calculation procedures for defined scattering and absorption quantities are provided in Appendix A. Here, we only briefly discuss our leaf scattering calculations, which are critical in understanding the scattering process.

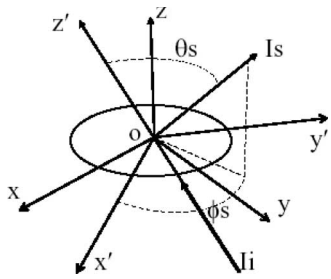


Fig. 1. Coordinate systems and leaf position used in this paper.

Fig. 1 illustrates the basic geometry of wave scattering by a leaf that lies on the $xy$ plane of the $xyz$ coordinates with the bottom of the leaf at $z = 0$. Also shown in this figure is the $x'y'z'$ coordinate system used in the derivation of the wave-scattering formulas and the incident intensity $I_i$ and scattered intensity $I_s$ of the EM fields. The $xyz$ and $x'y'z'$ coordinate systems share the same origin point o. The incidence direction is fixed in the positive $z'$ direction in the $x'y'z'$ coordinates. We assume that at the beginning of our simulation, the incident EM waves are normal to the leaf surface and propagate along the $z$-direction (i.e., the $x'y'z'$ coordinate system in this case overlaps with the $xyz$ coordinate system). Then, the $x'y'z'$ coordinate system rotates around o, so that a randomly incident direction can be achieved. Each spatial cell in our calculation is assigned to be $1/N$ of the wavelength of the incident wave, where $N$ is equal to 20 times the real part of the leaf refractive indexes and varies from $\sim$40 to $\sim$90 depending on the frequency and VWC. The large $N$ or small cell size used here is to account for quick changes of EM fields in spatial domains due to large leaf refraction at the SSM/I frequencies. The time step is set to be one half of the time that the wave can travel through a single cell. In the incident and all side directions, the computational domain is truncated by the UPML ABC (cf. Appendix A, [9], and [16] and [17]). The perfectly matched boundary layer absorbs all outgoing EM waves impinging on these boundaries and overcomes the artificial reflection from the boundaries. To obtain differential values of EM fields, magnetic and electric field components are alternatively evaluated at different temporal and spatial grid points with half time-step and half cell-size differences, respectively [cf. (A1a) and (A1b)].

Measurements [18] found that vegetation canopies could have various growth stages and very broad leaf angle distributions. These broad angle distributions indicate that random angle distributions of tree leaves may more realistically represent leaf orientations than a particular leaf angle in leaf

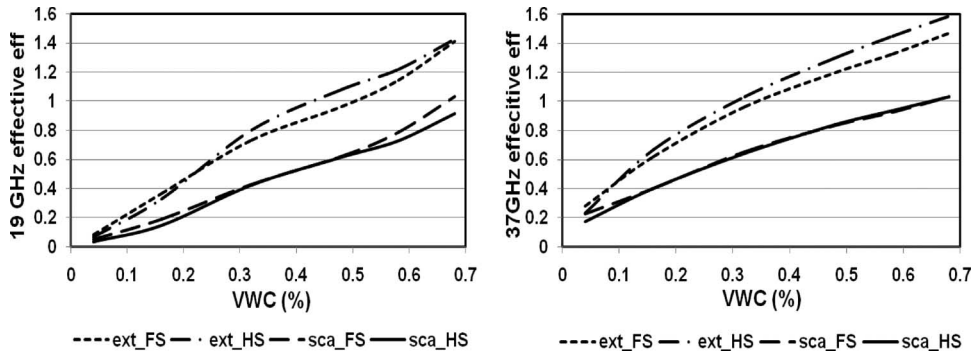


Fig. 2. Variations of effective efficiencies of extinction (ext) and scattering (sca) with VWC for FS and HS leaves at frequencies of (left) 19 GHz and (right) 37 GHz. The dotted, dash-dotted, dashed, and solid curves represent the results for the effective efficiencies of FS extinction, HS extinction, FS scattering, and HS scattering, respectively, as indicated in the figure.

scattering calculations for incident and scattered waves. Thus, the effect of randomly oriented natural leaves on scattering is simulated in this paper. Instead of changing the orientation angles of the assumed leaf in Fig. 1, we rotate the incident waves in both the zenith $\theta$ and azimuth $\phi$ angles (not shown in the figure) and compute the scattered EM fields and scattering properties for each sampled incidence direction. Our final scattering characteristics for the randomly oriented particles are the averages of all these scattering properties weighted by the spatial weights of incident angles, as discussed in [19]. Because of these calculations of randomly oriented leaves, the scattering characteristics can be simply described by the scattering angle (the angle between the incidence and scattering directions, i.e., the angle $\theta$s in Fig. 1). Since satellite microwave sensors, such as SSM/I, generally provide vertically (V) and/or horizontally (H) polarized radiation measurements, we transfer the $I$ and $Q$ components of the incident and scattered Stokes' vectors into the V and H components of the Stokes' parameters in this paper. The four elements in the Mueller matrix (or phase function matrix) that are directly related to these $I$ and $Q$ components are also correspondingly changed (cf. Appendix B) and named $P_{\rm VV}$, $P_{\rm VH}$, $P_{\rm HV}$, and $P_{\rm HH}$, as shown in the next sections. The $P_{\rm VV}$ and $P_{\rm HH}$ elements represent the leaf copolarization effects of the incident and scattered waves, whereas the other two elements describe those of cross polarization. Because there are almost no measurements of full Stokes' vectors from satellite microwave instruments, we only discuss these four elements of the phase function matrix in the following sections. The other elements in the phase function matrix are left for future studies.

## III. Results

Scattering characteristics are usually described by bidirectional distributions of the incident and scattered waves and the extinction and scattering of scattering objects (note that absorption is the difference between extinction and scattering). The bidirectional distributions are measured by the phase functions mentioned in the last section and in Appendix B. For the extinction and scattering, we use the effective efficiencies of extinction and scattering to quantify these physical properties, which are defined as the ratio of the extinction or scattering cross section to the elliptical area of the leaves, as shown in Fig. 1. Although the extinction or scattering cross section is generally a function of the incident angle and not a constant (cf. Appendix B), our calculated results for the randomly oriented disks do not depend on the incident angle and are only functions of the disk geometric and dielectric properties. That is, the effective efficiencies defined here are not variable with the incidence angle for each disk at a certain frequency. Thus, this definition of effective efficiencies can be easily used in microwave remote sensing applications for leaf extinction and scattering calculations.

Fig. 2 shows the variations of the effective efficiencies of extinction and scattering with VWC for the FS and HS leaves at frequencies of 19 GHz (left) and 37 GHz (right). In normal VWC dynamic ranges as calculated in this paper, these efficiencies essentially linearly vary with VWC. Although leaf moisture produces considerable absorption in the leaf scattering process, the higher the VWC, the stronger the extinction and scattering. The increases in the effective efficiencies of extinction and scattering of tree leaves with VWC are because both the real and imaginary parts of the refractive indexes of leaves increase with VWC. There is a factor of variation of about five to ten in these efficiencies. This large variability of extinction and scattering of tree leaves generates a great complexity in satellite remote sensing of vegetation canopies and makes the empirical estimations of VWC and vegetation–atmosphere interaction very difficult when emission signals from the canopies are used. From this figure, we can also find that the effective efficiencies, particularly the effective scattering efficiencies, at a given frequency are similar for both the FS and HS leaves, i.e., for a unit area, large and small leaves have almost the same scattering effects when these leaves are randomly oriented. Because the cross sections of extinction and scattering of tree leaves are the products of their corresponding effective efficiencies and the leaf areas, the actual extinction and scattering of the FS leaves are much higher than those of the HS leaves. This scattering feature of less size dependence is similar to that of absorbing spherical particles [20] when the size parameter $x = 2\pi a/\lambda$ is larger than 2. Here, $a$ is the radius of the spherical particle, and $\lambda$ is the wavelength of the incident wave. For our 19- and 37-GHz cases, when the long semiaxes of the FS and HS leaves are denoted as $a$, the values of the size parameter $2\pi a/\lambda$ are all above 2 and vary from about 5 to 20. Compared to those at 37 GHz, the effective

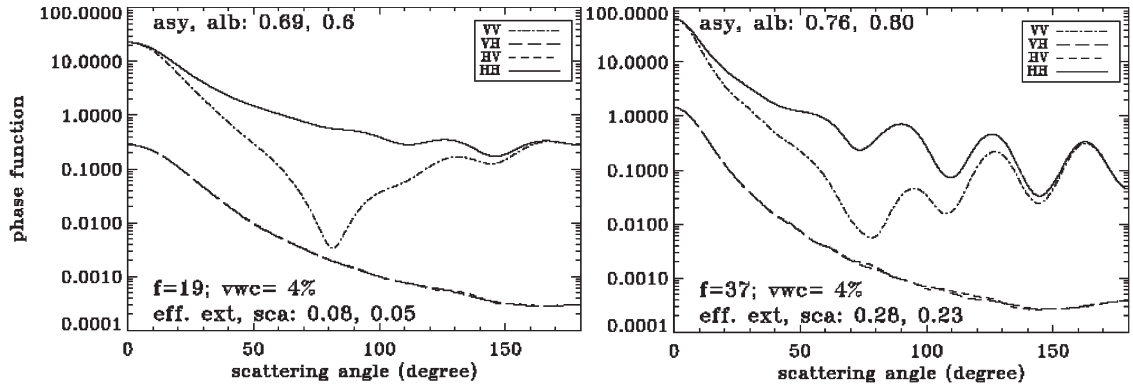


Fig. 3. Phase functions of leaf scattering for FS low-VWC (4%) leaves at both 19 and 37 GHz. Effective efficiencies of extinction and scattering, i.e., albedo (alb) and asymmetry factor (asy), are listed.

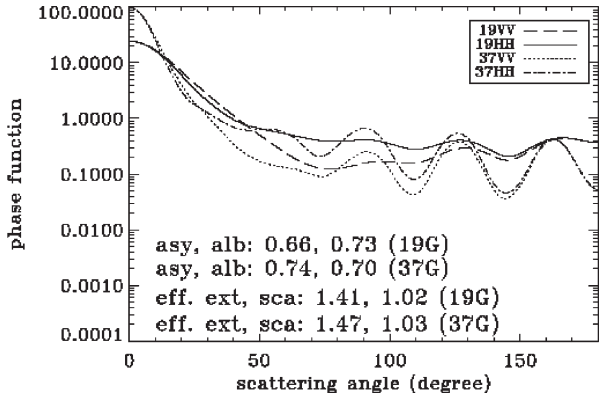


Fig. 4. Phase functions of copolarizations for FS leaves with 68% VWC.

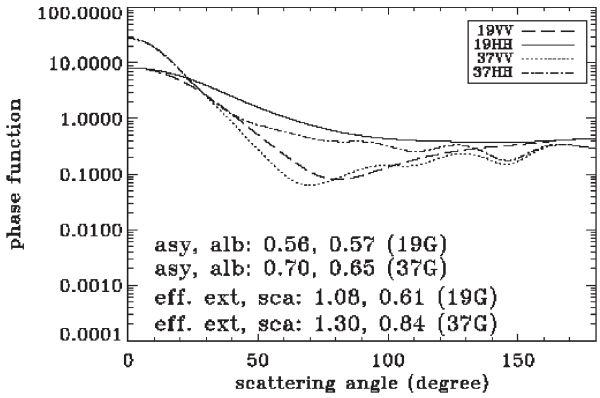


Fig. 5. Same as Fig. 4, but for HS leaves with 48% VWC.

efficiencies of scattering at 19 GHz are generally smaller, owing to the combined effects of the differences in size parameter and refractive index. The changes of effective efficiencies of extinction with VWC at both 19 and 37 GHz are greater than those for scattering because the absorption of leaves increases with increasing vegetation moisture. The single-scattering albedos and asymmetry factors of fresh leaves (not shown) have much less variability than the effective efficiencies of extinction and scattering and vary mostly from about 0.45 and 0.55, respectively, to $\sim$0.75. Generally, the albedo increases with increasing VWC. For dry leaves, their microwave absorption is significantly reduced due to dehydration; thus, the single-scattering albedos are enhanced (cf. Appendix B), particularly for the 37-GHz cases. The calculated moderate values of the asymmetry factor for elliptical disks are generally smaller than those for nonabsorbing large spherical particles and comparable to those for large absorbing spheres [10]. These moderate values of asymmetry factors indicate that leaves may have fairly strong side scattering and backscattering (see also Figs. 3–5), which provides good opportunities for monitoring vegetation canopies using off-nadir microwave satellite remote sensing techniques, such as SSM/I or synthetic aperture radar.

The phase functions of leaf scattering for low-VWC (4%) FS leaves are shown in Fig. 3, along with the calculated values for some important parameters, such as effective extinction (ext) and scattering (sca) efficiencies, single-scattering albedo (alb), and asymmetry factor (asy). As expected, cross-polarization values are much smaller than copolarization values at all scattering angles and for both the 19-GHz (left) and 37-GHz (right) cases. The overlap of the $P_{\rm VH}$ and $P_{\rm HV}$ curves in the figure reflects the symmetry of the two quantities and the accurate calculations of the FDTD model. This paper will not further discuss cross-polarization features and will only be focused on copolarization components.

When the scattering angle increases, the $P_{\rm HH}$ components of the phase function metrics are basically bigger than the $P_{\rm VV}$ components. The observed emissivity values at V polarization are higher than those at H polarization [2], [21] due to weaker reflectivity at this polarization, as shown here in its phase functions. At large scattering angles, both the $P_{\rm HH}$ and $P_{\rm VV}$ components at 19 GHz have noticeable oscillations with scattering angles. These oscillations are even significant at 37 GHz. When leaf moisture is increased to a high (68%) VWC value (i.e., in a stronger absorption case), this oscillation feature still shows up in the calculated results (Fig. 4). Similar $P_{\rm HH}$ and $P_{\rm VV}$ variations with scattering angles were also found in a study [5] of an idealized square vegetation disk for normal incident waves at 10 GHz. There are two oscillation peaks from both calculations located at scattering angles around 90° and 160°, although the third oscillation peak at a scattering angle of $\sim$125° obtained from this paper is not observed in [5]. In addition, the 15- to 20-dB intensity differences of scattered waves between forward scattering and those at these oscillation angles are generally consistent for both calculations

when the differences in wavelength, geometry of disks, and incident angle are considered. Thus, this oscillation feature, as that of large spherical particles, may be a general characteristic of large scattering disks at microwave wavelengths. Since the distributions of EM fields are basically decided by the interaction of the incident and scattered waves, the size parameters of both large and small dimensions of irregularly shaped scattering particles have significant influences on the scattering phase functions. Although FS leaves are generally thin for the SSM/I frequencies, the size parameters for both long and short semiaxes are large. Thus, the scattering effect for a large size parameter in our FS leaf cases shows up in the calculated results [20].

The scattering characteristics for HS leaves are generally similar to those for FS leaves, particularly for the 37-GHz cases, except that the magnitude of oscillations in large scattering angles is much smaller. Fig. 5 plots the phase functions of leaves with intermediate VWC (48%), in which case about half of the leaf weight is from water. The smooth feature at large scattering angles of the phase functions at 19 GHz is similar to that of small spheres [20] and is likely due to the smaller size parameters, particularly for the short semiaxis dimensions of the ellipse, compared to the FS cases, at the same wavelength. In the forward-scattering direction, the scattering phase functions at 37 GHz are considerably larger than those at 19 GHz, which is a scattering property that is typically observed for different particle size parameters.

To compare the current results with those obtained from an approximation similar to slab disks for a circular disk with a radius of 10 cm and a thickness of 0.5 cm by [14], we consider the calculations for HS leaves with a typical VWC of 48% (cf. Fig. 5). These calculations are chosen since the size parameters of [14] are similar to those of this paper. Despite the differences in the disk orientation (the random orientation for this paper versus the 30° incident angle in [14]), wavelength, and disk geometry, some general features in the scattering phase functions for both calculations are similar. The forward-scattering peaks of $P_{\mathrm{HH}}$ and $P_{\mathrm{VV}}$ are very strong and at least 20 times higher than those at 45° and other side-scattering angles. In addition, the bigger the size parameter and/or the larger the refractive indexes, the stronger the scattered waves (cf. Fig. 2). A significant difference between the scattered waves calculated in this paper and those in [14] is that there is a secondary scattering peak at an angle close to the specular reflection angle for specifically oriented disks, whereas the scattering phase functions for randomly oriented disks only have some oscillations at large scattering angles. Furthermore, the angular distributions of scattered energy for specifically oriented disks are very rough, which is a typical feature of physical optics. However, the changes in the phase functions of randomly oriented disks are generally smooth due to the averaging scattered fields among all disk orientation angles.

## IV. Summary

The single-scattering properties, i.e., the effective efficiencies of extinction and scattering, single-scattering albedo, asymmetry factor, and phases function, of tree leaves are critical parameters for modeling the emissivity and backscattering of vegetation canopies. However, research on these scattering properties is still in progress. This paper uses the FDTD method to numerically calculate accurate solutions of the single-scattering properties of randomly oriented leaves and evaluate the influence of VWC on these scattering properties at the 19- and 37-GHz SSM/I frequencies. The studied leaves are assumed to be thin elliptical disks with two different sizes and have various VWC values. The effective efficiencies of extinction and scattering defined and calculated in this paper may be useful in future microwave remote sensing of forest canopies. We find that leaf moisture not only produces considerable absorption but also increases scattering for tree leaves. The effective efficiencies of extinction and scattering essentially linearly increase with VWC with variations of a factor of five to ten at the considered wavelengths. The calculated asymmetry factors and phase functions indicate that the scattering at large scattering angles for broad leaves of deciduous trees could be strong, particularly at some special angles for certain sized leaves and wavelengths. Our calculated single-scattering properties, particularly the phase functions of tree leaves, lay the basic foundation for multiple-scattering calculations of forest radiation transfer and provide a great potential in quantifying the relations between satellite measurements and physical properties of vegetation canopies. To realize this, further studies on the scattering of different types of leaves, branches, and other forest elements, and evaluations of microwave radiative transfer processes within canopy layers are needed.

## Appendix A
## FDTD Technique With a UPML ABC

The FDTD technique with a UPML ABC used in this paper has been reported in previous studies [8]–[10]. We highlight critical features that are directly related to current calculations. More detailed discussions on the FDTD with UPML ABC can be found in [9].

### *FDTD Technique*

The FDTD technique calculates EM scattering and absorption in the time domain by directly solving the finite-differenced Maxwell's equations. The spatial and temporal derivatives of the electric and magnetic fields are approximated using a finite-difference scheme with spatial and temporal discretizations selected to limit the numerical dispersion errors and ensure numerical stability of the algorithm. The scatterer is embedded in a finite computational domain bounded by a truncation boundary. The EM properties of the scatterer and host medium are specified by assigning the permittivity, permeability, and conductivity at each grid point. A time-stepping iteration is used to simulate the field variation with time. The time series at each grid point is transformed into fields in the frequency domain using the discrete Fourier transform. The scattering and absorption quantities are calculated with fields in the frequency domain.

In a host medium (for this paper, it is free space), the explicit finite-difference approximation of Maxwell's equations is derived at discrete spatial and temporal points ($i$, $j$, $k$, and $n$) to sample the continuous space and time domains ($x$, $y$, $z$, and $t$), and the field components are calculated only at these discrete points. In a Cartesian grid system, the $x$ components of magnetic and electric fields are in the forms

$$\begin{aligned} &H_x^{n+1/2}(i,j+1/2,k+1/2) \\ &= H_x^{n-1/2}(i,j+1/2,k+1/2) \\ &\quad + \frac{\Delta t}{\mu(i,j+1/2,k+1/2)\Delta s} \\ &\quad \times \left[E_y^n(i,j+1/2,k+1) - E_y^n(i,j+1/2,k)\right. \\ &\qquad \left. + E_z^n(i,j,k+1/2) - E_z^n(i,j+1,k+1/2)\right] \end{aligned} \tag{A1a}$$

$$\begin{aligned} &E_x^{n+1}(i+1/2,j,k) \\ &= \exp\left[-\frac{\varepsilon_i(i+1/2,j,k)}{\varepsilon_r(i+1/2,j,k)}\omega\Delta t\right] E_x^n(i+1/2,j,k) \\ &\quad + \exp\left[-\frac{\varepsilon_i(i+1/2,j,k)}{\varepsilon_r(i+1/2,j,k)}\omega\Delta t/2\right] \frac{\Delta t}{\varepsilon_r(i+1/2,j,k)\Delta s} \\ &\quad \times \left[H_y^{n+1/2}(i+1/2,j,k-1/2)\right. \\ &\qquad - H_y^{n+1/2}(i+1/2,j,k+1/2) \\ &\qquad + H_z^{n+1/2}(i+1/2,j+1/2,k) \\ &\qquad \left. - H_z^{n+1/2}(i+1/2,j-1/2,k)\right] \end{aligned} \tag{A1b}$$

where $E_x$, $E_y$, $E_z$ and $H_x$, $H_y$, $H_z$ denote the electric and magnetic components, respectively. $\varepsilon_i$ ($\varepsilon_r$) and $\mu$ are the local imaginary (real) permittivity and permeability, respectively. $\omega$ is the angular frequency of the microwave. $\Delta s$ and $\Delta t$ represent the grid size and time increment, respectively. To guarantee the numerical stability of the FDTD technique, $\Delta t = \Delta s/2c$ is used, where $c$ is the light speed in free space. From (A1a) and (A1b), it can be seen that the magnetic and electric fields are on different spatial positions and are evaluated at alternating half-time steps. For FDTD grid points, the total- and scattered-field formulation is used to excite the magnetic and electric fields in the simulations of linearly polarized plane waves propagating in a finite region containing the analyzed disks, the host medium, and a UPML as the boundary condition.

### *UPML ABC*

In using the FDTD technique, to avoid artificial reflection from the truncation of the computational domain, the UPML developed in [16] is used. The UPML is a physical model based on an anisotropic perfectly matched medium. For a single interface, the anisotropic medium is uniaxial and is composed of both electric permittivity and magnetic permeability tensors. To match a UPML along a planar boundary to a lossy isotropic half-space characterized by permittivity $\varepsilon$ and conductivity $\sigma$, the time-harmonic Maxwell's equations can be written as

$$\nabla \times \mathbf{H}(x,y,z) = (i\omega\varepsilon + \sigma)\overline{\overline{s}}\mathbf{E}(x,y,z) \tag{A2a}$$

$$\nabla \times \mathbf{E}(x,y,z) = -i\omega\mu\overline{\overline{s}}\mathbf{H}(x,y,z) \tag{A2b}$$

where $\mathbf{H}$ and $\mathbf{E}$ denote the magnetic and electric field vectors, respectively, and $\overline{\overline{s}}$ is the diagonal tensor defined by

$$\begin{aligned} \overline{\overline{s}} &= \begin{bmatrix} s_x^{-1} & 0 & 0 \\ 0 & s_x & 0 \\ 0 & 0 & s_x \end{bmatrix} \begin{bmatrix} s_y & 0 & 0 \\ 0 & s_y^{-1} & 0 \\ 0 & 0 & s_y \end{bmatrix} \begin{bmatrix} s_z & 0 & 0 \\ 0 & s_z & 0 \\ 0 & 0 & s_z^{-1} \end{bmatrix} \\ &= \begin{bmatrix} s_y s_z s_x^{-1} & 0 & 0 \\ 0 & s_x s_z s_y^{-1} & 0 \\ 0 & 0 & s_x s_y s_z^{-1} \end{bmatrix} \end{aligned} \tag{A3}$$

where $s_x = \kappa_x + (\sigma_x/i\omega\varepsilon_0)$, $s_y = \kappa_y + (\sigma_y/i\omega\varepsilon_0)$, and $s_z = \kappa_z + (\sigma_z/i\omega\varepsilon_0)$. Note here that the UPML properties $(\kappa_x, \sigma_x)$, $(\kappa_y, \sigma_y)$, and $(\kappa_z, \sigma_z)$ are independent of medium permittivity $\varepsilon$ and conductivity $\sigma$, and are assigned to the FDTD grids in the UPML with the following strategies: 1) At the $x_{\min}$ and $x_{\max}$ boundaries, $\sigma_y = \sigma_z = 0$, and $\kappa_y = \kappa_z = 1$; at the $y_{\min}$ and $y_{\max}$ boundaries, $\sigma_x = \sigma_z = 0$, and $\kappa_x = \kappa_z = 1$; at the $z_{\min}$ and $z_{\max}$ boundaries, $\sigma_y = \sigma_x = 0$, and $\kappa_y = \kappa_x = 1$. 2) At $x_{\min}$, $x_{\max}$ and $y_{\min}$, $y_{\max}$ overlapping dihedral corners, $\sigma_z = 0$, and $\kappa_z = 1$; at $y_{\min}$, $y_{\max}$ and $z_{\min}$, $z_{\max}$ overlapping dihedral corners, $\sigma_x = 0$, and $\kappa_x = 1$; at $z_{\min}$, $z_{\max}$ and $x_{\min}$, $x_{\max}$ overlapping dihedral corners, $\sigma_y = 0$, and $\kappa_y = 1$. 3) At all overlapping trihedral corners, the complete general tensor in (A3) is used. 4) Smooth transition of the UPML material parameters with a polynomial grading function is used within the boundary layer for other intermediate points.

## APPENDIX B
## FORMULATION OF THE SINGLE-SCATTERING PROPERTIES

This section provides basic procedures to calculate the most important scattering parameters used in this paper. Detailed information on these parameters can be found in [9], [15], [20], and [22].

For wave scattering by particles in free space, the far-field approximation for the EM field is used to calculate the particle scattering and extinction cross sections. In the frequency domain, a complex Poynting vector, the flow of energy, and the direction of the EM wave propagation can be written as $\mathbf{s} = \mathbf{E} \times \mathbf{H}^*$, where the asterisk denotes the complex conjugate, and $\mathbf{E}$ and $\mathbf{H}$ are complex electric and magnetic fields, respectively. Thus, the energy absorbed by the particle is

$$\begin{aligned} w_a &= -\frac{1}{2}\mathrm{Re}\left[\oiint_s \mathbf{n}\cdot\mathbf{s}(\boldsymbol{\xi})d^2\xi\right] \\ &= -\frac{1}{2}\mathrm{Re}\left[\iiint_v \nabla\cdot\mathbf{s}(\boldsymbol{\xi})d^3\xi\right] \end{aligned}$$

$$= \frac{\omega}{2} \iiint_v \varepsilon_i(\boldsymbol{\xi}) \mathbf{E}(\boldsymbol{\xi}) \cdot \mathbf{E}^*(\boldsymbol{\xi}) d^3\xi \tag{B1}$$

where $\mathbf{n}$ denotes the outward-pointing unit vector normal to the particle surface. The surface and volume integrals are evaluated for the particle.

When EM waves are incident on a particle, the electric and magnetic field vectors $\mathbf{E}$ and $\mathbf{H}$ can be taken as sums of the incident and scattered fields. Consequently, the scattered field vectors can be written as

$$\mathbf{E}_s = \mathbf{E} - \mathbf{E}_i \tag{B2a}$$

$$\mathbf{H}_s = \mathbf{H} - \mathbf{H}_i \tag{B2b}$$

where $\mathbf{E}_i$ and $\mathbf{H}_i$ denote the incident electric and magnetic field vectors, respectively. Therefore, the rate of energy scattered by the particle can be taken as

$$\begin{aligned} w_s &= \frac{1}{2}\mathrm{Re}\left[\oiint_s \mathbf{n} \cdot (\mathbf{E}_s \times \mathbf{H}_s^*)\, d^2\xi\right] \\ &= \frac{1}{2}\mathrm{Re}\left\{\oiint_s \mathbf{n} \cdot [(\mathbf{E}-\mathbf{E}_i) \times (\mathbf{H}^*-\mathbf{H}_i^*)]\, d^2\xi\right\}. \end{aligned} \tag{B3}$$

Because both absorption and scattering remove energy from the incident waves, the extinction rate of the energy can be defined as

$$\begin{aligned} w_e &= w_s + w_a \\ &= \frac{1}{2}\,\mathrm{Re}\left\{\oiint_s \mathbf{n} \cdot [(\mathbf{E} - \mathbf{E}_i) \times (\mathbf{H}^* - \mathbf{H}_i^*)]\, d^2\xi\right\} \\ &\quad - \frac{1}{2}\,\mathrm{Re}\left[\oiint_s \mathbf{n} \cdot (\mathbf{E} \times \mathbf{H}^*) d^2\xi\right] \\ &= \frac{1}{2}\,\mathrm{Re}\left[\oiint_s \mathbf{n} \cdot (\mathbf{E}_i \times \mathbf{H}_i^* - \mathbf{E}_i \times \mathbf{H}^* - \mathbf{E} \times \mathbf{H}_i^*)\, d^2\xi\right] \\ &= \frac{1}{2}\,\mathrm{Re}\left[\iiint_v \nabla \cdot (\mathbf{E}_i \times \mathbf{H}_i^* - \mathbf{E}_i \times \mathbf{H}^* - \mathbf{E} \times \mathbf{H}_i^*)\, d^3\xi\right]. \end{aligned} \tag{B4}$$

Assuming that the rate of energy incident on a particle of arbitrary shape is $f$, then the absorption, scattering, and extinction efficiencies are $Q_a = w_a/f$, $Q_s = (w_e - w_a)/f$, and $Q_e = w_e/f$, respectively. The single-scattering albedo is consequently defined as $\tilde{\omega} = Q_s/Q_e$. Because $f$ is proportional to intensity $I$ of the incident wave and particle geometry shadow area $\Omega$ (i.e., $f = \Omega I$), the parameters previously mentioned can be calculated from current FDTD simulations. In a similar way, the extinction and scattering cross sections are defined as $Q_e^*\Omega$ and $Q_s^*\Omega$, respectively.

The scattering Mueller matrix (or phase function matrix) is calculated by using the four elements of the amplitude scattering matrix, as discussed in classical literature [19] and textbooks [22]. The asymmetry factor $g$ is the first moment of the phase function $P_{11}$, i.e.,

$$g = \frac{1}{2}\int_{-1}^{1} P_{11}(\cos\,\theta) \cos\,\theta\, d(\cos\,\theta) \tag{B5}$$

where $\theta$ is the scattering angle.

After obtaining the phase function matrix for the first two components of the Stokes' vectors, i.e., $I$ and $Q$, we transfer it into the phase function matrix for horizontally and vertically polarized waves. Since

$$\begin{aligned} \begin{bmatrix} I_s \\ Q_s \end{bmatrix} &= \begin{bmatrix} 1 & 1 \\ 1 & -1 \end{bmatrix} \begin{bmatrix} I_{\mathrm{hs}} \\ I_{\mathrm{vs}} \end{bmatrix} \\ &= \begin{bmatrix} P_{11} & P_{12} \\ P_{21} & P_{22} \end{bmatrix} \begin{bmatrix} I_i \\ Q_i \end{bmatrix} \\ &= \begin{bmatrix} P_{11} & P_{12} \\ P_{21} & P_{22} \end{bmatrix} \begin{bmatrix} 1 & 1 \\ 1 & -1 \end{bmatrix} \begin{bmatrix} I_{hi} \\ I_{vi} \end{bmatrix} \end{aligned} \tag{B6}$$

then

$$\begin{bmatrix} I_{\mathrm{hs}} \\ I_{\mathrm{vs}} \end{bmatrix} = \frac{1}{2} \begin{bmatrix} 1 & 1 \\ 1 & -1 \end{bmatrix} \begin{bmatrix} P_{11} & P_{12} \\ P_{21} & P_{22} \end{bmatrix} \begin{bmatrix} 1 & 1 \\ 1 & -1 \end{bmatrix} \begin{bmatrix} I_{hi} \\ I_{vi} \end{bmatrix} \tag{B7}$$

where $P_{11}$, $P_{12}$, $P_{21}$, and $P_{22}$ are the four elements of the phase function matrix for the $I$ and $Q$ components. The subscripts i and s represent the incident and scattered waves, whereas the subscripts h and v are for the horizontal and vertical polarizations, respectively. Thus, the scattering phase functions of linearly polarized components can be expressed as

$$\begin{bmatrix} P_{\mathrm{HH}} & P_{\mathrm{VH}} \\ P_{\mathrm{HV}} & P_{\mathrm{VV}} \end{bmatrix} = \frac{1}{2} \begin{bmatrix} 1 & 1 \\ 1 & -1 \end{bmatrix} \begin{bmatrix} P_{11} & P_{12} \\ P_{21} & P_{22} \end{bmatrix} \begin{bmatrix} 1 & 1 \\ 1 & -1 \end{bmatrix} \tag{B8}$$

where $P_{\mathrm{HH}}$, $P_{\mathrm{HV}}$, $P_{\mathrm{VH}}$, and $P_{\mathrm{VV}}$ are the four elements of the phase function matrix for the horizontally and vertically polarized components.

## ACKNOWLEDGMENT

The authors would like to thank W. Rossow, E. Njoku, G. Gibson, and D. Garber for their valuable comments.

## REFERENCES


[1] C. Bertrand, N. Clerbaux, A. Ipe, S. Dewitte, and L. Gonzalez, "Angular distribution models, anisotropic correction factors, and mixed clear-scene types: A sensitivity study," *IEEE Trans. Geosci. Remote Sens.*, vol. 43, no. 1, pp. 92–102, Jan. 2005.

[2] Q. Min and B. Lin, "Remote sensing of evapotranspiration and carbon uptake at Harvard Forest," *Remote Sens. Environ.*, vol. 100, no. 3, pp. 379–387, Feb. 2006.

[3] Q. Min and B. Lin, "Determination of spring onset and growing season leaf development using satellite measurements," *Remote Sens. Environ.*, vol. 104, no. 1, pp. 96–102, Sep. 2006.

[4] K. Saleh, A. Porte, D. Guyon, P. Ferrazzoli, and J.-P. Wigneron, "A forest geometric description of a maritime pine forest suitable for discrete microwave models," *IEEE Trans. Geosci. Remote Sens.*, vol. 43, no. 9, pp. 2024–2035, Sep. 2005.

[5] I. Koh and K. Sarabandi, "A new approximate solution for scattering by thin dielectric disks of arbitrary size and shape," *IEEE Trans. Antennas Propag.*, vol. 53, no. 6, pp. 1920–1926, Jun. 2005.

[6] Y. C. Lin and K. Sarabandi, "Monte Carlo coherent scattering model for forest canopies using fractal-generated trees," *IEEE Trans. Geosci. Remote Sens.*, vol. 37, no. 1, pp. 440–451, Jan. 1999.

[7] I. Koh and K. Sarabandi, "Polarimetric channel characterization of foliage for performance assessment of GPS receivers under tree canopies," *IEEE Trans. Antennas Propag.*, vol. 50, no. 5, pp. 713–726, May 2002.

[8] W. Sun, G. Videen, B. Lin, and Y. Hu, "Modeling light scattered from and transmitted through dielectric periodic structures on a substrate," *Appl. Opt.*, vol. 46, no. 7, pp. 1150–1156, 2007.

[9] W. Sun, N. G. Loeb, and Q. Fu, "Finite-difference time domain solution of light scattering and absorption by particles in an absorbing medium," *Appl. Opt.*, vol. 41, no. 27, pp. 5728–5743, 2002.

[10] W. Sun, Q. Fu, and Z. Chen, "Finite-difference time domain solution of light scattering by dielectric particles with a perfectly matched layer absorbing boundary condition," *Appl. Opt.*, vol. 38, no. 15, pp. 3141–3151, 1999.

[11] M. El-Rayes and F. Ulaby, "Microwave dielectric spectrum of vegetation—Part I: Experimental observations," *IEEE Trans. Geosci. Remote Sens.*, vol. GRS-25, no. 5, pp. 541–549, Sep. 1987.

[12] F. Ulaby and M. El-Rayes, "Microwave dielectric spectrum of vegetation—Part II: Dual-dispersion model," *IEEE Trans. Geosci. Remote Sens.*, vol. 25, no. 5, pp. 550–557, Sep. 1987.

[13] H. T. Cuah, K. Y. Lee, and T. W. Lau, "Dielectric constants of rubber and oil palm leaf samples at X-band," *IEEE Trans. Geosci. Remote Sens.*, vol. 33, no. 1, pp. 221–223, Jan. 1995.

[14] D. M. Le Vine, R. Meneghini, R. H. Lang, and S. S. Seker, "Scattering from arbitrarily oriented dielectric disks in the physical optics regime," *J. Opt. Soc. Amer.*, vol. 73, no. 10, pp. 1255–1262, Oct. 1983.

[15] M. A. Karam, "Bridging the quasi-static and the physical optics approximations: An elliptic disk case," *Appl. Opt.*, vol. 37, no. 9, pp. 1666–1673, 1998.

[16] Z. S. Sacks, D. M. Kingsland, R. Lee, and J.-F. Lee, "A perfectly matched anisotropic absorber for use as an absorbing boundary condition," *IEEE Trans. Antennas Propag.*, vol. 43, no. 12, pp. 1460–1463, Dec. 1995.

[17] S. D. Gedney, "An anisotropic perfectly matched layer-absorbing medium for the truncation of FDTD lattices," *IEEE Trans. Antennas Propag.*, vol. 44, no. 12, pp. 1630–1639, Dec. 1996.

[18] W. Huang, Z. Niu, J. Wang, L. Liu, C. Zhao, and Q. Liu, "Identifying crop leaf angle distribution based on two-temporal and bidirectional canopy reflectance," *IEEE Trans. Geosci. Remote Sens.*, vol. 44, no. 12, pp. 3601–3609, Dec. 2006.

[19] M. Mishchenko, L. Travis, and A. Lacis, *Scattering, Absorption, and Emission of Light by Small Particles*. Cambridge, U.K.: Cambridge Univ. Press, 2002.

[20] J. Hansen and L. Travis, "Light scattering in planetary atmospheres," *Space Sci. Rev.*, vol. 16, no. 4, pp. 52–610, Oct. 1974.

[21] B. Lin and P. Minnis, "Temporal variations of land surface microwave emissivities over the ARM southern great plains site," *J. Appl. Meteorol.*, vol. 39, no. 7, pp. 1103–1116, Jul. 2000.

[22] C. F. Bohren and D. R. Huffman, *Absorption and Scattering of Light by Small Particles*. New York: Wiley, 1983.



**Bing Lin**, photograph and biography not available at the time of publication.

**Wenbo Sun**, photograph and biography not available at the time of publication.

**Qilong Min**, photograph and biography not available at the time of publication.

**Yongxiang Hu**, photograph and biography not available at the time of publication.